J Solid State Electrochem (2009) 13:283–291
DOI 10.1007/s10008-007-0488-9

ORIGINAL PAPER

Effect of hydrostatic extrusion on passivity breakdown on 303 austenitic stainless steel in chloride solution

M. Pisarek · P. Kędzierzawski · M. Janik-Czachor · K. J. Kurzydłowski

Received: 30 September 2007 / Revised: 7 November 2007 / Accepted: 28 November 2007 / Published online: 10 January 2008

Abstract The stability of the passive film formed on austenitic 303 stainless steel in the as-received state and after severe plastic deformation by hydrostatic extrusion (HE) leading to nanostructurization was investigated in an aggressive environment containing Cl^- ions by anodic polarization. Transmission electron microscopy (TEM) and stereological image analysis were used to examine structural changes introduced by HE. Surface analytical techniques such as light microscopy, scanning electron microscopy, Auger electron spectroscopy (AES), and scanning Auger microscopy (SAM) were used to characterize the morphology, grain size, and chemistry of the surface, including local characterization of nonmetallic inclusions and their surface before and after HE. SAM analysis revealed discontinuities of the passive oxide film on MnS inclusions. TEM and scanning transmission electron microscopy examinations confirm a drastic reduction of grain size accompanied by a distinct refinement of the size of sulfide inclusions in the HE matrix. These changes in the HE 303 stainless steel are apparently responsible for its reduced pitting resistance compared to the as-received material.

Contribution to the Fall Meeting of the European Materials Research Society, Symposium D: 9th International Symposium on Electrochemical–Chemical Reactivity of Metastable Materials, Warsaw, 17th–21st September, 2007.

M. Pisarek (✉) · P. Kędzierzawski · M. Janik-Czachor
Institute of Physical Chemistry, Polish Academy of Sciences,
Kasprzaka 44/52,
01–224 Warsaw, Poland
e-mail: marcinp@ichf.edu.pl

M. Pisarek · K. J. Kurzydłowski
Faculty of Materials Science and Engineering,
Warsaw University of Technology,
Woloska 141,
02–507 Warsaw, Poland

Keywords Austenitic stainless steel · Severe plastic deformation · Hydrostatic extrusion · Nanomaterials · Nonmetallic inclusions · Anodic polarization · Surface oxide film · Passivity · Pit nucleation · SEM · TEM · AES · Ion sputtering

Introduction

Stainless steels are frequently used as construction materials for service in aggressive environments. Their generally excellent resistance to corrosion is due to the spontaneous formation of a protective passive surface film, only a few nanometers thick. There is a general agreement that these thin films are enriched in chromium with respect to the bulk composition [1–4]. The passive films formed on austenitic steel when exposed to aqueous solutions are a mixture of iron and chromium oxides, with hydroxide and water-containing compounds concentrated in the outermost region of the film, with chromium oxide enrichment at the metal–film interface.

It is known that the stability of the passive state is not determined by the overall composition of the passive film but is limited by the susceptibility of passive alloys such as stainless steel to pitting or crevice corrosion in the presence of chloride ions. Chemical inhomogeneities, especially nonmetallic inclusions, have long been shown to act as nucleation sites for pitting attack [5–8].

Pitting corrosion of stainless steel is known to be strongly influenced by a variety of internal factors such as composition and microstructure as well as the external parameters: chemistry, pH, and temperature of the particular environment. The role of impurity inclusions, especially MnS inclusions, in triggering pitting corrosion of commercial stainless steels has long been recognized. Many

investigations have been carried out to determine the details of the effect of these inclusions on corrosion resistance [5, 7]. It has also been pointed out that the presence of MnS inclusions on the surface can lead to discontinuities of the passive film, exposing the inclusions/matrix boundaries directly to the environment [6]. From the chemical point of view, the explanations of the role of MnS inclusions in pitting corrosion proposed so far are based on the low stability of MnS in acidic solutions and the detrimental effect of the dissolution products of the sulfides. However, it should be mentioned also that the size and geometry of MnS inclusions are expected to influence propagation or repassivation of a pit nucleus. Because of their small size, the composition and chemical state of the inclusions' components were rather difficult to determine precisely. A high-resolution local characterization technique is needed to determine the chemistry of the inclusions and, thereby, to gain an insight into their role in the stability of the passive state. Scanning Auger microscopy (SAM) is a suitable technique for this purpose because it is surface sensitive. The technique provides information limited to a depth of 1 nm or less [9–11]. Simultaneously, lateral resolution of ~20 nm can be obtained.

Nanostructured materials have attracted the attention of scientists and engineers because of their specific physical and mechanical properties [12–15]. One of the methods developed so far to successfully produce a nanostructured material is hydrostatic extrusion (HE), which enables the fabrication of bulk nanocrystalline materials [16]. It is worth noting that hydrostatic extrusion is one of the methods by which a homogenous microstructure is obtained within the entire volume of the processed material. This process is characterized by high strain rates at a relatively low temperature. The plastic deformation process can be carried out in one step or accumulatively, step by step.

Much work have been carried out to study the physical and mechanical properties of nanostructured Al, Al-based alloys, Ti, Cu, Ni, and stainless steel [17–21]. However, the corrosion properties, including the stability of the naturally occurring passivating oxide film, of such technically important materials as HE stainless steel materials are not well understood. Severe plastic deformation introduced by HE may cause significant changes in the corrosion resistance. In particular, a large plastic strain will be introduced, the overall length of grain boundaries will be multiplied, and their structure and composition may change.

The 303 austenitic stainless steel with an appropriate sulfur content to enhance its machinability is frequently used as a free-machining alloy. The good resistance of the material to atmospheric corrosion and to many chemicals, combined with a high machinability, makes it suitable for general applications in mechanical industries.

While there is a voluminous literature concerning the passivity and pitting [1–4, 22–28] of stainless steels including 303 austenitic stainless steel, it is reasonable to undertake investigations using the same experimental conditions before and after the HE to gain an insight into the effect of hydroextrusion on the corrosion resistance.

This paper reports on the anodic behavior of 303 austenitic stainless steel before and after hydrostatic extrusion, which has been studied by potentiostatic and potentiodynamic polarization measurements in chloride-containing solutions at room temperature. The microstructure of the as-received material (before HE) was examined by light microscopy and by transmission electron microscopy (TEM) after processing by HE. The chemical composition of the passive film and nonmetallic inclusions within the matrix were determined using Auger electron spectroscopy (AES) technique.

The aim of this study was to characterize the effect of HE process on the passivity breakdown in 303 stainless steel.

Experimental

Materials

Commercial-quality 303 austenitic stainless steel was used for the investigations. Its chemical composition is given in Table 1 (wt.%). The atomic concentration of the main components is also given.

The concentration of metallic elements (Fe, Cr, Ni, Mn, Mo, Cu) was examined by a X-MET 3000T Metorex X-ray spectrometer. For the surface and bulk analytical investigations in the initial state, samples were cut from rods as discs with a diameter of 9.5 mm and a height of about 8 mm.

The 303 rods, with an initial diameter of 9.5 mm, were hydrostatically extruded using carbon-rich compression medium, by multi-step process, to a final diameter of 3.4 mm, which corresponds to a true strain of 2.05 (ε=

Table 1 Composition of 303 stainless steel

	Fe	Cr	Mn	Ni	Mo	Cu	Si	P	S	C
Wt.%	Balance	17.5	2.0	8.5	0.4	0.6	1.0 max	0.2 max	0.35 max	0.15 max
At.%	Balance	18.3	2.0	7.9	0.2	0.5	1.9 max	0.4 max	0.6 max	0.7 max

2.05). The principles of hydrostatic extrusion are presented elsewhere [12, 16]. A billet of the test material is extruded through a die, located in the operational chamber. During the hydrostatic extrusion process, the piston does not contact the charge material and, in the deformation zone of the die (the cone), the material itself flows on a film of lubricant under the applied pressure (hydrodynamic lubrication). Very low friction allows for severe deformations in the range of 2.0 (see [12, 16] for details).

The samples were polished with emery grade from 360 to 1,200 and finished with aluminum paste abrasive slurry (ϕ=1 μm), rinsed with distilled water, washed with acetone, and exposed to air for 3 days.

A central part of the hydroextruded rods was used for the investigations.

Bulk and surface analytical investigations

Microstructure and surface topography examination

The microstructure of commercial 303 stainless steel was examined by light microscopy, whereas the nano-structure of the HE specimens was examined by scanning transmission electron microscope (Jeol JEM 1200EX, 120 kV) and high-resolution scanning microscope with a STEM mode (bright field—BF, Hitachi S-5500, 30 kV). Thin foils for TEM examinations were cut from the rods perpendicular to the extrusion direction and thinned electrochemically by a standard method in acidic solution (95% concentrated acetic acid+5% perchloric acid).

The two-dimensional (2D) diameter of nonmetallic inclusions was measured using software for image analysis (MicroMeter, copyright by T. Wejrzanowski [29]). The equivalent 2D diameter of individual inclusions was determined as the radius of circle having a surface area equivalent to the 2D surface area of a given inclusion. Statistical approximations were carried out to estimate the mean value of the inclusions' diameter, E (d_2). The image analysis program was able to distinguish between the inclusions with the diameter in the range of 0.1–1.7 μm with the resolution of about 0.05 μm.

Surface analytical investigations—Auger electron spectroscopy

A high-resolution scanning Auger microprobe, Microlab 350 (Thermo Electron—Thermo VG Scientific), equipped with field-emission electron gun (FEG-tip) and Ar^+ ion gun (EX05) was used for the AES analysis.

The austenitic steel samples were examined with AES to determine the composition and estimate the thickness of the surface oxide film. Discontinuous sputtering (4-s etching steps) was used to gradually remove the oxide films. The sputtering parameters were: ion energy 3 keV, beam current 1 μA, and crater size 16 mm^2. The Auger spectra were recorded, after each sputtering period, at a primary energy E=10 keV. Ion etching of a reference tantalum sample covered by a Ta_2O_5 layer of known thickness has shown that the sputtering rate was about 0.1 nm/s.

A scanning Auger microprobe was used to monitor the surface morphology (SEM) and local chemical composition, utilizing SAM functions of the instrument with a lateral resolution of about 20 nm. The detailed lateral distribution of elements was examined utilizing the Auger line scan function. The chemical state of surface species was identified using the high-energy resolution analyzer (the energy resolution of the analyzer is continuously variable between 0.6% and 0.06%) and the appropriate standards. The conversion of the Auger signals into atomic concentration of the components was undertaken by using sensitivity factors S_f from the Thermo VG Scientific database and by adopting non-linear least square fitting procedure to deconvolute Fe and Mn peaks for MnS inclusion.

An Avantage-based data system software (version 3.44) was used for data acquisition and processing.

Electrochemical measurements

Anodic polarization curves and current density vs. time curves at E=const. were recorded in borate buffer+0.1 M NaCl (pH 8.4) at room temperature (25 °C). This solution is commonly used to study a material's resistance to pitting. A fresh solution, de-aerated with nitrogen, was used for each experiment. An EP 20 potentiostat with an EG 20 function generator from ELPAN was used in the standard three-electrode configuration. A normal silver chloride electrode (Ag/AgCl/1 M KCl)—recalculated to normal calomel electrode (Hg/Hg_2Cl_2/1 M KCl) (NCE) scale which is 0.04 V more positive than the SCE scale—and a platinum wire electrode were used as reference and counter electrodes, respectively.

Immediately after placing the sample in the electrochemical cell, a constant potential was applied by stepping to E=const.< E_{np}' and the anodic current was monitored with time. A Faraday cage was used to protect the electrochemical cell from external noise signals.

A slow potential sweep rate of 1 V/h was applied for the potentiodynamic experiments. Positive potentiodynamic scans were initiated from −0.8 V_{NCE} (−0.76 V_{SCE}) until the current density reached 1 mA/cm^2. (This procedure was adopted after Yang and Mcdonald [36], who used it for similar measurements for 316 stainless steel in order to improve reproducibility.) The apparent pitting potential, E_{np}', was estimated from the anodic polarization curves. The authors are aware, however, that E_{np}' may be some 100 mV more positive than the true pitting potential

because the induction period for pit nucleation is potential dependent [25].

Results and discussion

Internal structure

The light microscopy image (Fig. 1a) reveals the typical microstructure of 303 stainless steel in as-received state; the deformation twins and numerous small nonmetallic inclusions are visible. The grain size is in the range of 20–40 μm, which is typical for an austenitic stainless steel. Figure 1b presents a STEM-BF image of the same material after HE process. It is evident that HE has produced a major reduction of the grain size. The elongated nano-grains ("domain structure") of ~10–20 nm width are well visible. The image reveals deformation twins in the primary austenite. The twins intersect each other at various angles, forming characteristic blocks—a specific structure on nanometric scale. Figure 1c shows the TEM micrographs of HE 303 steel. An insert in the upper right corner of the image presents the selected area diffraction pattern (SAD). One can observe characteristic strong diffraction rings consisting of "spot-like" reflections with the reflections being distinctly stronger in certain directions. The latter case suggests the formation of a textured material. SAD pattern obtained for several other samples were very similar. Apparently, the diffracted beams became scattered into ring characteristic of polycrystalline materials, as the grain boundary misorientation significantly increased. These results imply the presence of many small grains within the area excited by the incident electron beam. Thus, the HE procedure resulted in an average reduction of grain size by a factor of ~10^3. Evidently, due to severe deformation during HE, a textured material was formed.

Nonmetallic inclusions

Examinations of the 303 stainless steel microstructure revealed that there was a large number of nonmetallic inclusions within the grains and at the grain boundaries.

Figure 2 shows results of image analysis for the inclusions in the as-received (a) and HE-processed materials (b). About 260 inclusions were present at the surface in the area taken for the stereological analysis in the as-received material. However, the number of inclusions in the 303 after HE was much larger and, therefore, the area examined was 1/25 as large as that of as-received material. In this case, about 130 inclusions with the equivalent diameter from 0.1 to 1.7 μm were taken into account. A rough estimation suggests that the number of inclusions per unit area after HE increased by a factor of 16. The mean values of equivalent diameters E (d_2) of the inclusions are 0.66 and 0.25 μm in as-received and HE-treated material, respectively. Careful inspection of the HE 303 steel samples suggests that inclusions with a diameter below 0.1 μm are also present. However, they are below the resolution of the image analysis program used in this investigation. Despite the drawbacks of the method

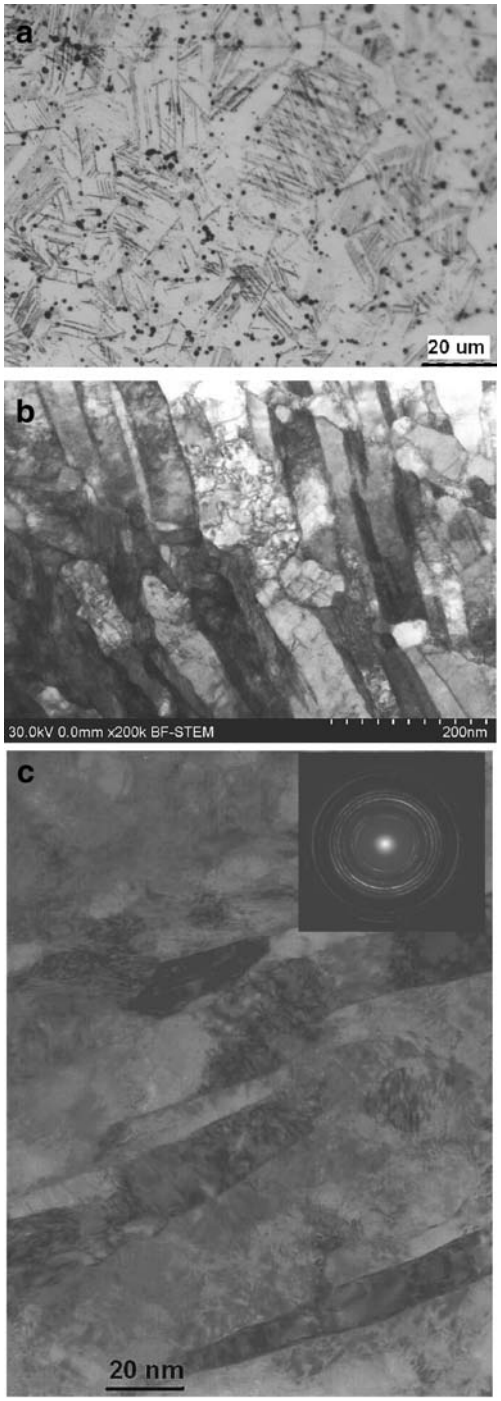

Fig. 1 Microstructure of 303 austenitic stainless steel **a** in as-received state (the deformation twins and many small nonmetallic inclusions are visible), **b** after hydrostatic extrusion (SEM-BF image). **c** Transmission electron micrographs of 303 stainless steel after hydroextrusion process; in an *insert* the selected area diffraction pattern is also given

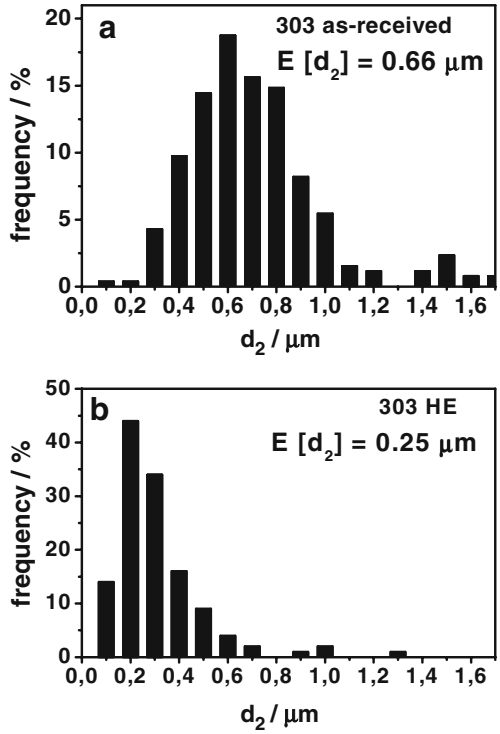

Fig. 2 Results of image analysis performed for the inclusions in as-received material (**a**) and after the HE process (**b**). d_2—two-dimensional equivalent diameter of non-metallic inclusions, present at the surface, determined as the radius of circle having a surface area equivalent to the two-dimensional surface area of a given inclusion. $E[d_2]$ the mean value of the equivalent inclusions' diameter as estimated form a statistical approximation. See text for details

applied, it is evident that the HE pretreatment reduces the size of inclusions and apparently increases their total number per unit volume.

Figure 3a shows a SEM image of 303 sample surfaces after mechanical polishing, without etching. Two local Auger spectra (Fig. 3b), taken from the inclusion's center (marked on the SEM image) and from the substrate, reveal that the inclusion is enriched with Mn and S. The high-resolution Auger spectrum of Mn taken from the inclusion (Fig. 3c) confirms that Mn is bound to S there. For comparison, a high-resolution elemental Mn (LMM) reference spectrum is also given.

To obtain a semi-quantitative distribution of elements within a typical inclusion, a line scan analysis was performed across the inclusion or steel interface (see an example in Fig. 4). The line scan indicates that the inclusion not only consists mainly of manganese and sulfur (at equal proportions suggesting MnS) but also contains a certain amount of chromium and nickel. However, one cannot exclude the fact that the inclusion is sufficiently thin to let attenuated signals of Cr and Ni from the matrix reach the detector.

There is a lot of discussion in literature on the role of nonmetallic inclusions in stainless steels [25, 30–35] in causing a reduction of the corrosion resistance. There is a general agreement that MnS_x inclusions are the most harmful. The main reasons for their detrimental role, pointed out by different authors, are:

- chemical instability in acidic solutions [30]
- presence of voids or crevices at the inclusion/matrix boundaries [31–35]
- absence or lower stability of the passivating film formed on the inclusions locally [32, 34] as compared to the passivating film on the matrix

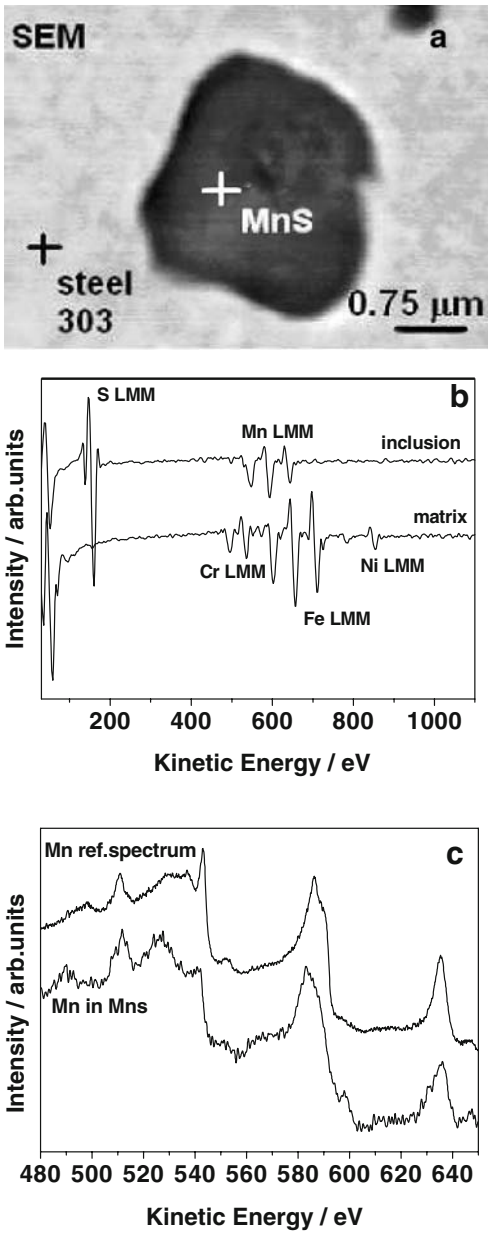

Fig. 3 **a** SEM image of 303 stainless steel's surface in as-received state. Spots of local AES analysis are marked. **b** Differential Auger spectra from inclusion and the matrix taken for identification of chemical composition. **c** High-resolution AES spectra showing the position and shape of Mn (*LMM*) Auger signal from the MnS inclusion. Reference spectrum for elemental Mn (*LMM*) is also given

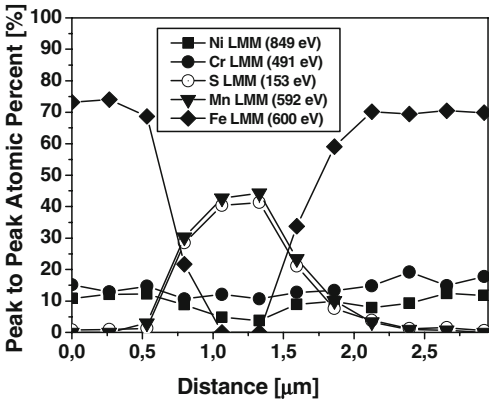

Fig. 4 Auger line analysis recorded across a MnS inclusion. Atomic concentrations of Mn and S in the inclusion are equal, confirming a stoichiometric MnS compound

The results presented below suggest that the latter effect is prevailing.

Surface oxide film

The mapping function of Microlab 350 gives the possibility of checking whether or not the surface oxide film protecting the steel substrate from the aggressive action of the environment is equally present on the surface of the substrate and on the sulfide inclusions occurring at the surface. The SAM measurements confirmed that there is always a discontinuity within the passivating film on the MnS inclusions in the as-received 303 stainless steel as shown in Fig. 5. The distribution image of Auger O KLL signals from the surface shows unambiguously that there is a lack of oxygen within this surface region, where S LMM Auger signal shows the presence of manganese sulfide inclusion. It is, therefore, clear that this region and its boundary with the matrix are more prone to Cl^- attack than the matrix itself.

To obtain the internal composition of the oxide film covering the metal matrix, composition profiles were measured using AES and Ar^+ ion sputtering technique.

Figure 6a shows a typical composition profile of air-formed film on 303 stainless steel, as measured with AES combined with Ar^+ ion sputtering. The surface oxide is evidently contaminated with carbon, which, however, can be easily removed from the surface after several seconds of sputtering. As seen from Fig. 6a, the film consists of oxygen, chromium, iron, and nickel. The film gets removed after ~36 s of sputtering, which corresponds to a thickness of about 3.6 nm, based on a sputtering rate of 0.1 nm/s. Similar composition profiles are obtained for the HE-processed material (Fig. 6b). The film seems to be thicker (about 5.6 nm) than before HE, as one can judge from the decrease of O KLL signal down to 33% of its maximum value. Although this result for 303 HE is well reproducible, it is worth double checking (with another experimental technique) whether this estimation of thickness based only on the sputtering time is correct. The main differences are:

- a considerable contamination of the surface oxide with carbon for the alloy after HE, which may be a result of the HE process (see "Experimental" section).
- a larger enrichment in Cr for 303 HE. This is highlighted in Fig. 6c, which demonstrates the depth profiles of the relative Cr/Fe atomic concentration.

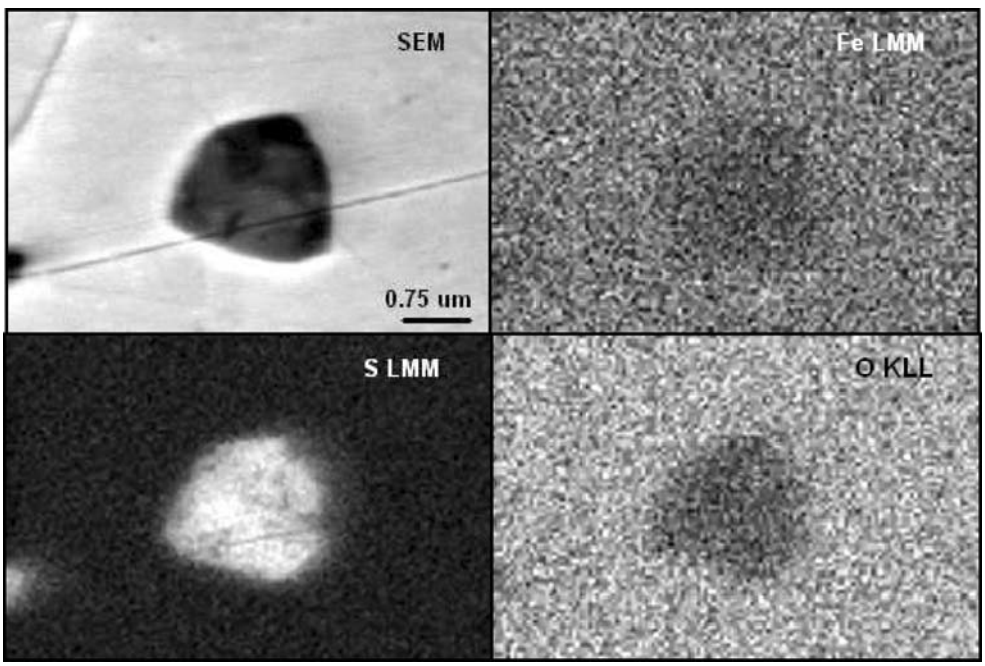

Fig. 5 SEM images and distribution images of elements: Fe (*LMM*), S (*LMM*), and O (*KLL*) on the surface of 303 stainless steel before HE process, suggesting a distinct depletion of oxygen on the surface of sulfide inclusion

The data show that the maximum Cr/Fe concentration ratio within the film reaches ~0.5 for 303 HE, whereas it reaches ~0.4 only for 303 in the as-received state. Apparently, the hydrostatic extrusion may result in an enhancement of the migration of components to the surface of the metastable matrix containing a larger density of grain boundaries, dislocations, etc., thus, leading to a higher enrichment of chromium within the surface oxide film on HE substrate. Some differences in the degree of chromium enrichment in the surface film due to different samples' pretreatment were already reported [37].

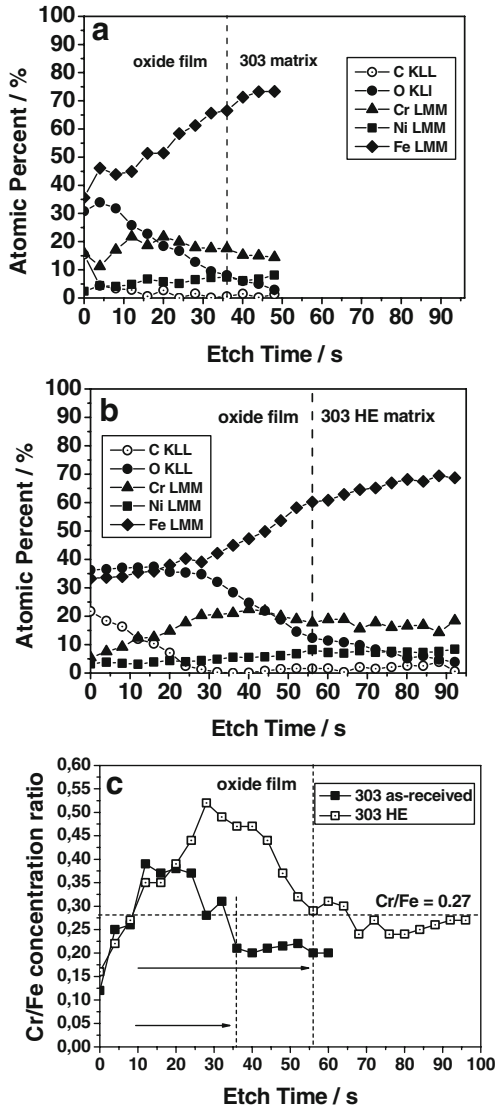

Fig. 6 Depth composition profiles of an oxide film formed in air on 316 stainless steel in an initial state (**a**) and after hydrostatic extrusion (**b**). Comparison of relative atomic concentration ratio of Cr/Fe vs. sputtering time for both states. Bulk Cr/Fe atomic concentration ratio is also marked

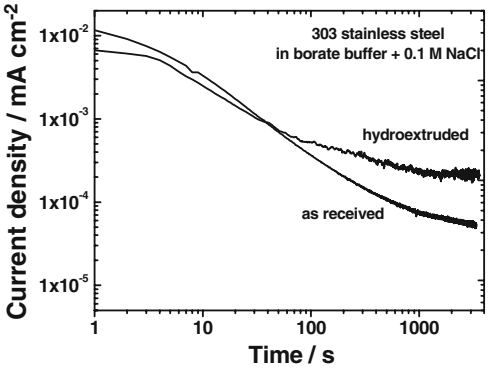

Fig. 7 Lg c.d. vs. lg time curves, at E=0.0 V_{NCE} for 303 stainless steel: in as-received state and after hydrostatic extrusion

Effect of Cl^- ions on pit nucleation

Figure 7 illustrates the effect of HE on the kinetics of passivation of 303 stainless steel at a constant potential below the breakdown potential. The 'as-received' material exhibits the typical passivation behavior with a slope of lg i vs. lg t equal to about −1 [38]. The HE 303 exhibits a different behavior. The current density decreases more slowly with time than for the as-received material in spite of the higher Cr content in the surface film (see Fig. 6b) which is expected to improve passivity. It is not possible at present to suggest a satisfactory explanation of this behavior. Certainly, a different mechanism for growth of the passive film on the HE material is operating here. The new model of the mechanism should consider the metastable state of the HE matrix, possessing heavy plastic strain and a huge number of grain boundaries and dislocations which may form rapid diffusion or migration paths. To separate the effects of grain refinement from those of a heavy plastic strain on passivity, a future research is planned on HE samples subjected to a controlled heat treatment.

Figure 8 summarizes potentiodynamic polarization measurements for 303 samples air-exposed after mechanical polishing, in borate buffer solution + 0.1 M NaCl, before and after HE. The current density within the passive region for the as-received material exhibits a gradual increase, reaching 4.0±0.5 μA/cm^2 just before the breakdown. The sudden increase in the current density by over a factor of 50 at potentials above E_{np}'=0.28±0.02 V_{NCE} is due to pit nucleation and growth. The 303 stainless steel in as-received state exhibits a good reproducibility of the current density within the stable passivity region. Anodic polarization curves for HE 303 steel in the same solution (in contrast to the behavior of the as-received material) exhibit a stable, potential independent, current density of about 6 μA/cm^2, which is thus higher than for the as-received material. The material undergoes a breakdown of passivity at E_{np}'=0.22±0.04 V_{NCE}. These results suggest

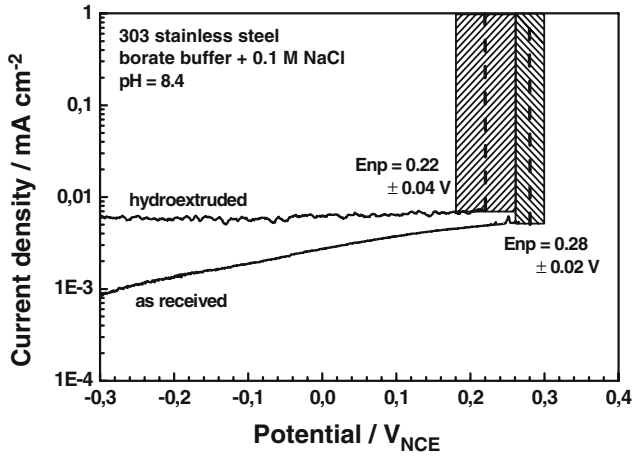

Fig. 8 Potentiodynamic polarization curves of 303 stainless steel before and after HE, measured in borate buffer solution containing 0.1 M NaCl (see text for details). Scan rate 1 V/h. *Dotted line*—mean value of the breakdown potential, E_{np}. *Stripped area*—mean error range

that a large population of small sulfide inclusions may affect the behavior of HE 303 steel more than the larger MnS sulfides in the as-received material do, thus shifting the apparent breakdown potential E_{np}' to lower values. This may be ascribed to the effects of the sulfide inclusions and the associated effects discussed already in literature [33, 34]. The present data show a tendency of 303 HE to pit at somewhat lower anodic potentials than the as-received material does. This behavior is a result of two overlapping effects*: a larger number and a smaller size of MnS inclusions in 303 HE* (see "Nonmetallic inclusions" and Fig. 2). It is difficult to decide at present which of them prevails. Further research is required on a series of carefully prepared alloys with a controlled amount of S and Mn to obtain materials differing in the number of MnS inclusions, but not in their size.

Microscopic examinations confirm that pits are formed preferentially at the MnS inclusions present in the as-received 303 or in the HE-pretreated material. Figure 9a and b shows a typical example of a HE 303 steel surface after anodic polarization in Cl^--containing solution (compare Fig. 8). Corrosion attack is visible around the inclusion. It is thus not reasonable to relate the corrosion attack to nano-grains in the bulk HE 303 steel as the nonmetallic inclusions present large (micrometer size) and frequent heterogeneities in the material investigated which dominate pit nucleation process in the subtle nanostructure of HE 303 steel.

The present results point to the role of MnS inclusions in the process of passivity breakdown mostly due to the discontinuities of the passivating oxide film on these inclusions (compare Fig. 5). It is worth noting that the 316 stainless steel, where MnS inclusions are absent, exhibits distinct extension of its stable passivity region after the HE process [39].

Conclusion

- Microscopic and TEM experiments have revealed that HE resulted in a drastic change in the structure of 303 stainless steel. The grain size was reduced by a factor of ~10^3, and a strongly textured material was obtained.
- TEM and stereological image analysis have revealed that HE resulted in a reduction in the size of nonmetallic sulfide inclusions by a factor of 3.5 times or more.
- Air-formed film on as-received material is thinner than that on HE-pretreated material (as estimated from the AES-Ar^+ ion depth profiling experiments). Moreover, there are distinct differences in chemical composition. The HE 303 substrate is covered with an air-formed film enriched with Cr to a greater extent than that on the as-received material.
- SAM microanalytical investigations revealed local discontinuities within the passivating oxide film over the sulfide inclusions at the surface; such discontinuities provide a direct contact between the boundary inclusions/matrix and the aggressive environment.
- The values of apparent breakdown potential E_{np}' suggest that the HE 303 tends to be less resistant to pitting in buffered Cl^- solution than the as-received material. This is ascribed to the larger density of local

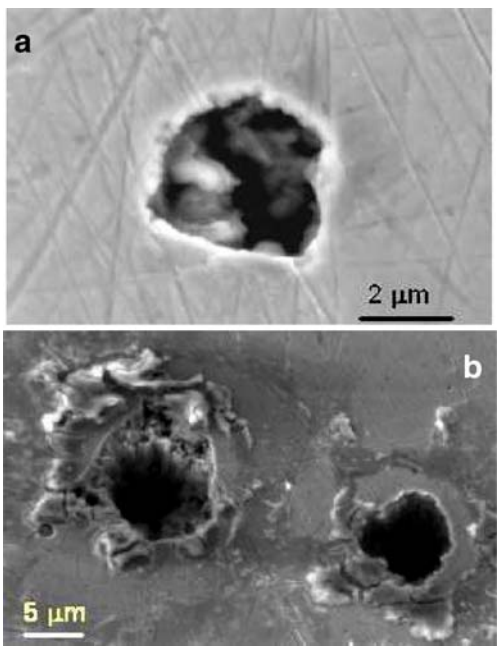

Fig. 9 **a**, **b** Typical example of a HE 303 steel surface after anodic polarization in Cl^--containing solution. Corrosion attack around the inclusion is well visible

discontinuities within the surface oxide film due to a considerably higher density of sulfide inclusions in the HE 303 steel compared to the as-received material.

– The general conclusion from this investigation is that structural changes (including nanostructurization) introduced by hydrostatic extrusion and the following "homogenization" of the material appear inefficient in improving the resistance to pit nucleation of the steels containing MnS inclusions (in contrast to those which do not contain the MnS inclusions in their structure). Even after the size reduction, the MnS inclusions do not undergo passivation, thus providing a large number of susceptible spots for passivity breakdown in a chloride-containing environment.

Acknowledgement The authors are grateful to Prof. A. Szummer, Prof. K. Hashimoto, and Dr. T. Wejrzanowski for helpful discussions. This work was financially supported by the Polish Ministry of Education and Science through grant 3T08C 013 29 and by the Foundation for Polish Science through a generous fellowship for M. Pisarek. Surface characterizations were performed using a Microlab 350 located at the Physical Chemistry of Materials Center of the Institute of Physical Chemistry, Polish Academy of Sciences and of the Faculty of Materials Science and Engineering, Warsaw University of Technology.

References

1. Frankenthal RP, Kruger J (eds) (1978) Chapter: Stainless steels and ferrous alloys. Passivity of metals. ECS, Princeton, pp 646–770
2. Sato N, Hashimoto K (eds) (1990) Chapter: Stainless steels. Passivation of metals and semiconductors. The sixth international symposium on passivity, Sapporo, Japan, 1989. Pergamon Press, Oxford, pp 515–591
3. Heusler KE (ed) (1995) Chapter: The passivity of metal. Passivation of metals and semiconductors. Special issue of Mater Sci Forum 185–188:221–364
4. Natishan PM, Isaacs HS, Janik-Czachor M, Macagano VA, Marcus P, Seo M (eds) (1998) Chapter: Chemistry and structure of passive oxide films on iron and its alloys. Passivity and its breakdown. ECS, Pennington, pp 143–285
5. Rossi A, Elsener B, Hahner G, Textor M, Spencer ND (2000) Surf Interface Anal 29:460
6. Janik-Czachor M (1995) Mater Sci Forum 1:185
7. Schmuki P, Hildebrand H, Freidrich A, Virtanen S (2005) Corros Sci 47:1239
8. Vuillemin B, Philippe X, Oltra R, Vignal V, Coudreuse L, Dufour LC, Finot E (2003) Corros Sci 45:1143
9. Reniers F, Tewell C (2005) J Electron Spectrosc 142:1
10. Briggs D, Grant JT (2003) Surface analysis by Auger and X-ray photoelectron spectroscopy, Surface Spectra. IM, Chichester
11. Watts JF, Wolstenholme J (2003) An introduction to surface analysis by XPS and AES. Wiley, England
12. Kurzydłowski KJ (2004) Bull Pol Acad Sci Tech Sci 52(4):301
13. Ivanisienko Yuv, Korznikov AV, Safarov IM, Valiev RZ (1995) Nanostruct Mater 6:433
14. Suś-Ryszkowska M, Wejrzanowski T, Pakieła Z, Kurzydłowski KJ (2004) Mat Sci Eng A 369:151
15. Valiev RZ, Alexandrov IV (1999) Nanostruct Mater 12:35
16. Hung JCh, Hung Ch (2000) J Mater Process Technol 104:226
17. Lewandowska M (2006) J Microsc 224:34
18. Garbacz H, Lewandowska M, Pachla W, Kurzydłowski KJ (2006) J Microsc 223:272
19. Budniak J, Lewandowska M, Pachla W, Kulczyk M, Kurzydłowski KJ (2006) Solid State Phenom 114:57
20. Zhang Z, Akiyama E, Watanabe Y, Katada Y, Tsuzaki K (2007) Corros Sci 49:2962
21. Krasilnikov K, Lojkowski W, Pakiela Z, Valiev R (2005) Mat Sci Eng A 397:330
22. Bastidas JM, Torres CL, Cano E, Polo JL (2002) Corros Sci 44:625
23. Shih CC, Shih CM, Su YY, Su LHJ, Chang MS, Lin SJ (2004) Corros Sci 46:427
24. Hashimoto K, Asami K (1978) In: Frankenthal RP, Kruger J (eds) Passivity of metals. ECS, Princeton, New Jersey, p 749
25. Janik-Czachor M (1981) J Electrochem Soc 128:513C
26. Janik-Czachor M, Wood GC, Thompson GE (1980) Brit Cor J 15:154
27. Engell HJ, Oriani RA (1989) Corros Sci 29:119
28. Lumsden JB, Staehle RW (1972) Scripta Mat 6:1205
29. Wejrzanowski T (2000) Computer assisted quantitative description of the functionally graded materials. Master's thesis, Warsaw University of Technology
30. Eklund GS (1974) J Electrochem Soc 121:467
31. Scotto J, Ventura G, Traverso E (1979) Corros Sci 19:237
32. Szummer A, Janik-Czachor M, Hofmann S (1994) In: Marcus P, Baroux B, Keddam M (eds) Proceedings of European symposium on modification of passive films. vol. 12. Institute of Materials, London, p 280
33. Jansen EFM, Sloof WG, de Wit JHW (1994) In: Marcus P, Baroux B, Keddam M (eds) Proceedings of European symposium on modification of passive films. vol. 12. Institute of Materials, London, p 290
34. Janik-Czachor M, Szummer A (1993) Corrosion Review 11:118
35. Baroux B, Gorse G (1994) In: Marcus P, Baroux B, Keddam M (eds) Proceedings of European symposium on modification of passive films. vol. 12. Institute of Materials, London, p 300
36. Yang S, Mcdonald DD (2007) Electrochim Acta 52:1871
37. Okamoto G, Shibata T (1978) In: Frankenthal RP, Kruger J (eds) Passivity of metals. ECS, Princeton, New Jersey, p 646
38. Kirchheim R (1987) Electrochim Acta 32:1619
39. Pisarek M, Kędzierzawski P, Janik-Czachor M, Kurzydłowski KJ (2008) Corrosion NACE. In press